the
abdus salam
international centre for theoretical physics

40th anniversary 1964 2004

H4.SMR/1586-5

**"7th Workshop on Three-Dimensional Modelling
of Seismic Waves Generation and their Propagation"**

25 October - 5 November 2004

Higher Mode Tomography and Applications of 3D Models for Event Location

A. L. Levshin

**University of Colorado
Boulder, U.S.A.**

A. L. Levshin

University of Colorado, Boulder, U.S.A.

Higher Mode Tomography and Applications of 3D Models for Event Location

There are two separate aspects I will discuss at this lecture: (1) surface wave tomography using higher crustal modes; (2) use of 3D global model obtained by the surface wave tomography for relocation of seismic events.

1 Surface wave tomography using higher crustal modes

1.1 Introduction

Surface wave observations are commonly used to study crustal and upper mantle structures on local, regional and global scales. Tomographic inversions of surface wave travel times for two-dimensional (2-D) group and phase speed maps and three-dimensional (3-D) shear velocity structures are the subjects of numerous studies (e.g., Trampert & Woodhouse, 1995; Ekström et al., 1997; Shapiro & Ritzwoller, 2002; and many others). Central Asia has been a particular focus for these studies (e.g., Bourjot & Romanowicz, 1992; Wu & Levshin, 1994; Curtis & Woodhouse, 1997; Wu et al., 1997; Ritzwoller & Levshin, 1998; Ritzwoller et al., 1998; Griot et al., 1998; Huang et al., 2003; Shapiro et al., 2004), as it presents a mosaic of tectonic structures that result from the complex deformation history of the region. Because crustal structure is so varied across Central Asia, the ability to resolve the structure of the crust from the mantle is particularly problematic.

There are a number of approaches to surface wave tomography used in previous studies. Most are based on extracting dispersion information for fundamental Rayleigh and Love waves for a set of periods usually followed by a series of one-dimensional (1-D) inversions on a grid of locations for crustal and upper mantle shear velocities (e.g., Shapiro & Ritzwoller, 2002). Some authors (van Heijst & Woodhouse, 1999; Yoshizawa & Kennett, 2002) have also used higher mode phase velocities obtained by stripping these modes from the observed records. Another approach is based on full waveform fitting using synthetic seismograms for 1-D structures between source and receiver, and interpolating the estimated cross-sections to produce a 3-D model of the region of study (Nolet, 1978, 1987; Lebedev & Nolet, 2003; Friederich, 2003). Both of these approaches to introduce overtones into the inversion are applied at periods above 30 s where the overtones dominantly constrain mantle structure. The use of mantle overtones does not particularly help to improve estimates of crustal structure or to resolve the crust from the mantle. Crustal overtones at periods below 15-20 s, however, present information about crustal structure, that, if used together with fundamental mode data, may significantly improve estimates of the structure of the crust and resolution from the underlying mantle.

There have been several studies that demonstrated the observability and usefulness of crustal higher modes (e.g., Oliver & Ewing, 1957, 1958; Oliver et al., 1959; Oliver, 1962; Alexander, 1962;
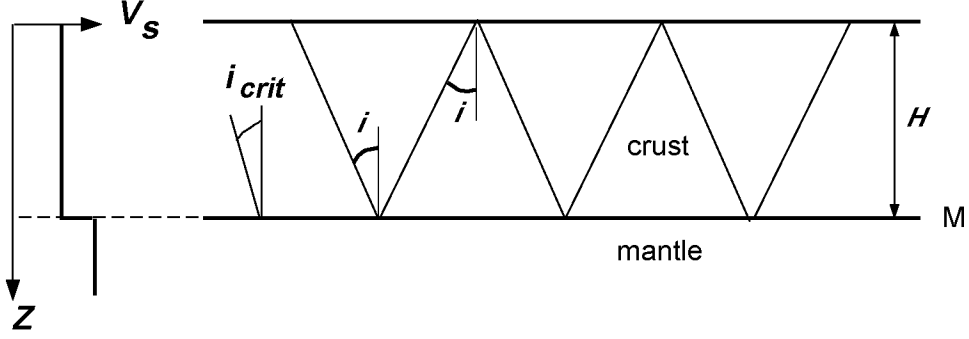
Figure 1: Multiple reflection of shear waves in a homogeneous crust as the physical basis for crustal overtones. The incidence angle $i > i_{crit}$.

Brune & Dorman, 1963, Kovach and Anderson, 1964; Crampin, 1964, 1966a, 1966b; Crampin & King, 1977; Nolet, 1975, 1977). For the most part, these studies have been confined to the interpretation of a small number of particular paths. To our knowledge, there has been no attempt to use crustal higher modes in tomographic inversions. Higher mode data have also been used in a completely different frequency range (2 - 15 Hz) to study the shear velocity structure of sediments in the top few tens of meters beneath the surface and the sea floor (e.g., Gabriels et al., 1987; Ritzwoller & Levshin, 2002).

In this lecture I will show the feasibility of introducing crustal overtone measurements to improve estimates of crustal structure within the context of a tomographic inversion.

1.2 Physical background

Let us briefly discuss the nature of crustal higher modes and their basic properties: expected dispersion, attenuation, amplitude spectra, excitation and radiation patterns as functions of source parameters. These results form the basis for our concentration on observing the first higher-modes across Central Asia.

1.2.1 The nature of crustal higher modes

Crustal higher modes result from the constructive interference of overcritical multiply reflected shear waves in the Earth's crust. The simplest reflection scheme is shown in Figure 1, where a one-layered homogeneous crust of thickness H with longitudinal and shear velocities Vp_1 and Vs_1 is underlain by a homogeneous half-space with velocities Vp_2 and Vs_2 ($Vp_1 > Vs_2 > Vs_1$). The reflection angle is always above the critical value $i_{\text{crit}} = \sin^{-1}(Vs_1/Vs_2)$, and both SH and SV waves are multiply reflected from the surface and the internal interface. This explanation of the generation of higher modes is confirmed by comparing the phase velocity curves obtained by solving the full eigenvalue problems for Love and Rayleigh waves (Woodhouse, 1988) with the equations obtained from the condition of constructive interference for multiply reflected shear waves (e.g., Ewing et al., 1957; Officer, 1958):

$$\frac{2H \cos i}{Vs_1} + \frac{T \arg(R_{SH}(i))}{2\pi} = nT \quad (n = 0, 1, 2, ..) \tag{1}$$

for Love waves, and

$$\frac{2H\cos i}{Vs_1} + \frac{T[\arg(R_{SV}(i)) + \arg(R0_{SV}(i))]}{2\pi} = nT \quad (n = 1, 2, ..) \tag{2}$$

for Rayleigh waves. Here i is the angle of incidence, $i = \sin^{-1}(Vs_1/C_n(T))$, $C_n(T)$ is the phase velocity for the nth mode at period T, R_{SH} and R_{SV} are the complex reflection coefficients of the corresponding waves from the internal interface, $R0_{SV}$ is the complex reflection coefficient for the SV wave from the free surface, and arg is a function that denotes the phase of a complex number. Note that $|R_{SV}| = |R0_{SV}| = |R_{SH}| = 1$. For this simple model, the techniques provides the same results for all modes except the fundamental Rayleigh mode ($n = 0$) whose phase velocity cannot be found from equation (2) because this mode includes the boundary Rayleigh wave which exists even in a homogeneous half-space.

In reality, the structure of the crust and upper mantle is more complicated than in this simple example, and the equations above do not describe the details of wave behavior. However, the presence of a strong velocity contrast at the Moho discontinuity, with inequalities $Vp_{cr} > Vs_M > Vs_{cr}$, where Vp_{cr} and Vs_{cr} characterize average velocities in the crust, and Vs_M is the shear velocity directly beneath the Moho, implies that this interpretation of the nature of crustal higher modes is reasonable on average. From equations (1) and (2), it is evident that crustal thickness and crustal and uppermost mantle shear velocities are the principal factors that determine the behavior of the higher mode dispersion curves.

1.2.2 Dispersion of higher crustal modes

To illustrate the influence of crustal structure on the dispersion of crustal higher modes for different structural and tectonic provinces, one-dimensional vertical profiles from a 3-D seismic model (Shapiro & Ritzwoller, 2002) at selected locations are used. The selected shear-velocity profiles are presented in Figure 2. Group velocity curves for Rayleigh and Love waves for the fundamental mode and the first several overtones are presented in Figure 3. Note that the second and higher overtone speeds for Rayleigh and Love waves are similar and are, therefore, hard to separate and measure directly. Parts of the fundamental and first overtone modes, however, are well separated from other modes and are measurable. This is the reason I focus on observations of the first Rayleigh and Love crustal overtones in addition to the fundamental modes. Further inspection of Figure 3 reveals that at short periods (< 5 sec), the group velocity of the Love modes and the Rayleigh modes with the exception of the fundamental mode asymptotically approach the minimum shear speed in the crust. (In fact, phase and group speeds are the same in the high frequency limit.) At this location in Kazakhstan, the model of Shapiro & Ritzwoller (2002) has no sediments and that speed is about 3.6 km/sec, the shear speed of the uppermost part of the crystalline crust. At longer periods, the Rayleigh and Love overtones superpose to form a guided whispering gallery wave in the uppermost mantle, directly beneath the Moho. The period band of sensitivity to crustal thickness and shear speeds in the body of the crust is represented by the part of the dispersion curves with a large slope (between the uppermost crustal modes and mantle whispering gallery modes). This part of the first overtone branch occurs between the Airy phase between about 5-10 sec period and about 18 sec period for Rayleigh waves and from about 10 sec to 15 sec period for Love waves. The exact period range will depend on the local structure, as the details of dispersion will vary from place to place. This is illustrated in Figure 4 which shows phase and group velocity curves from about 4 sec to 25 sec period for the four models at
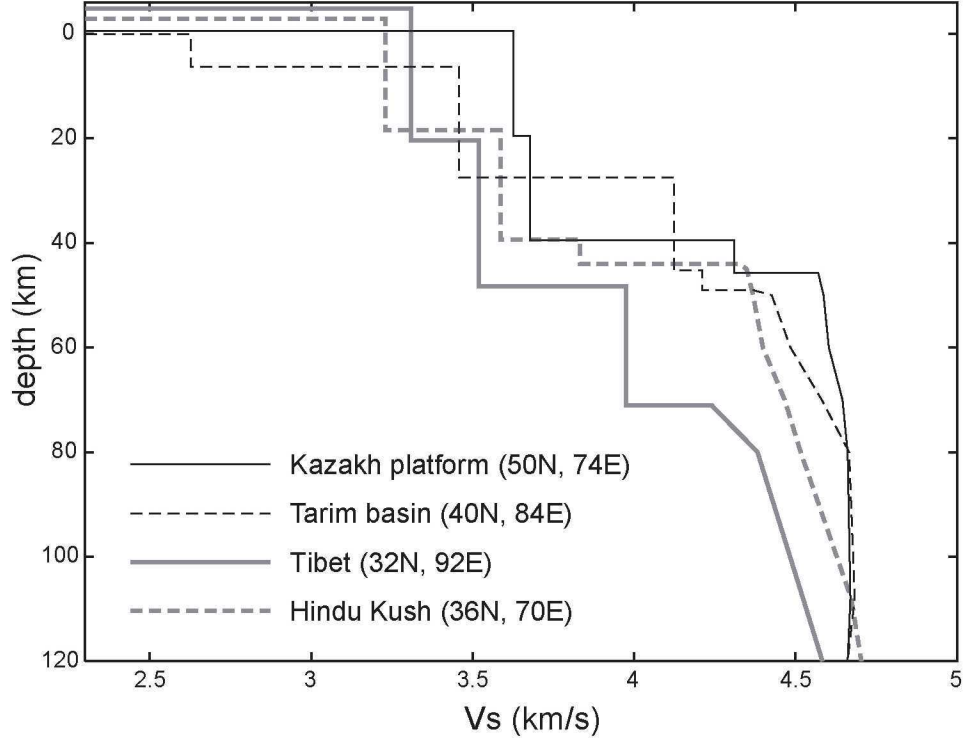
Figure 2: Shear velocity profiles for a variety of locations in Central Asia taken from the 3-D model of Shapiro and Ritzwoller (2002).

the locations in Figure 2. Note, in particular, how the period of the Airy phase seen in the group velocity of the first higher Rayleigh mode shifts to longer periods for the regions with thicker crust. In regions of thick crusts, the first higher mode dispersion curve is stretched horizontally to longer periods relative to regions with thinner crust. This is a fundamental observable that can be used to constrain crustal properties. Sensitivity kernels for phase and group velocities to perturbations in shear velocity as a function of depth at periods between 7 sec and 15 sec for the Tibetan plateau (Fig. 2) are shown in Figure 5. The maximum sensitivity at these periods is in the middle crust, at depths between 20 and 60 km for Tibet. For shield areas, maximum sensitivity is between 10 to 40 km. Sensitivity deepens as period increases. The group velocity sensitivity kernels usually have two lobes: a positive lobe in the upper crust and a negative lobe in the lower crust. The sensitivity kernels for phase velocity have only a positive lobe. Group velocity maxima are usually 1.5 to 2.0 times larger in magnitude than the maxima for the phase velocity kernels.

1.2.3 Amplitudes: modal Q and excitation of higher modes

The observability of the first overtone will depend on its absolute amplitude, and its amplitude relative to the fundamental mode. Its absolute amplitude depends in part on its modal quality factor, Q^*, which we show here increases with crustal thickness. We also show that its amplitude, both in absolute and relative terms, improves with deeper events.

The attenuation of higher modes is described by the modal Q value, $Q^*(T)$, which depends on the intrinsic Q profile of the crust and uppermost mantle and the depth of penetration of the modal
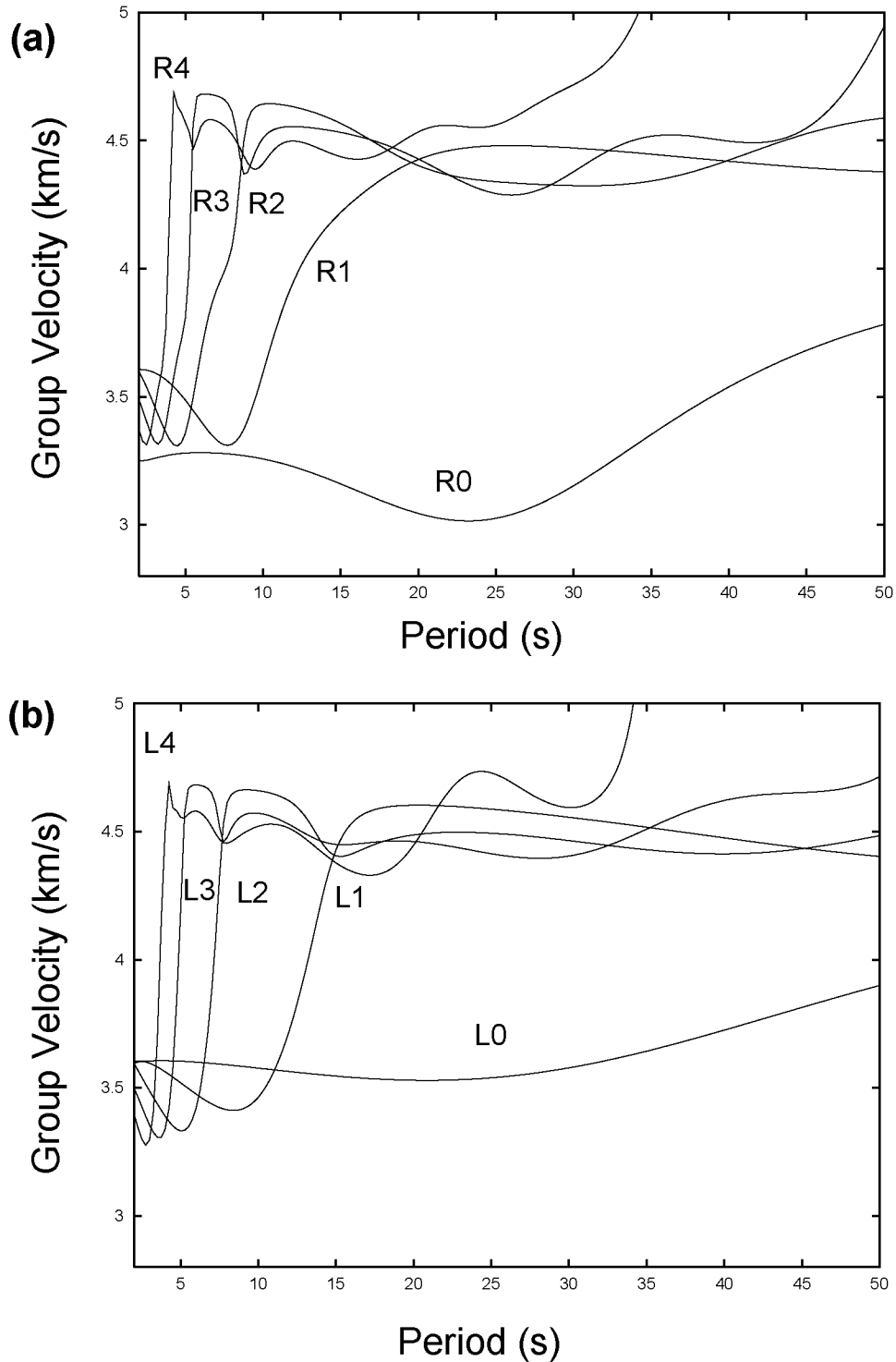
4

Figure 3: Group velocity curves at a point within the Kazakh Platform (same location as the vertical profile shown in Figure 2 taken from Shapiro and Ritzwoller, 2002), computed using the method of Woodhouse (1988). (a) Rayleigh waves for the fundamental mode (R_0), and the first through fourth higher modes ($R_1 - R_4$). (b) Love waves for the fundamental mode (L_0), and the first through fourth higher modes ($L_1 - L_4$).
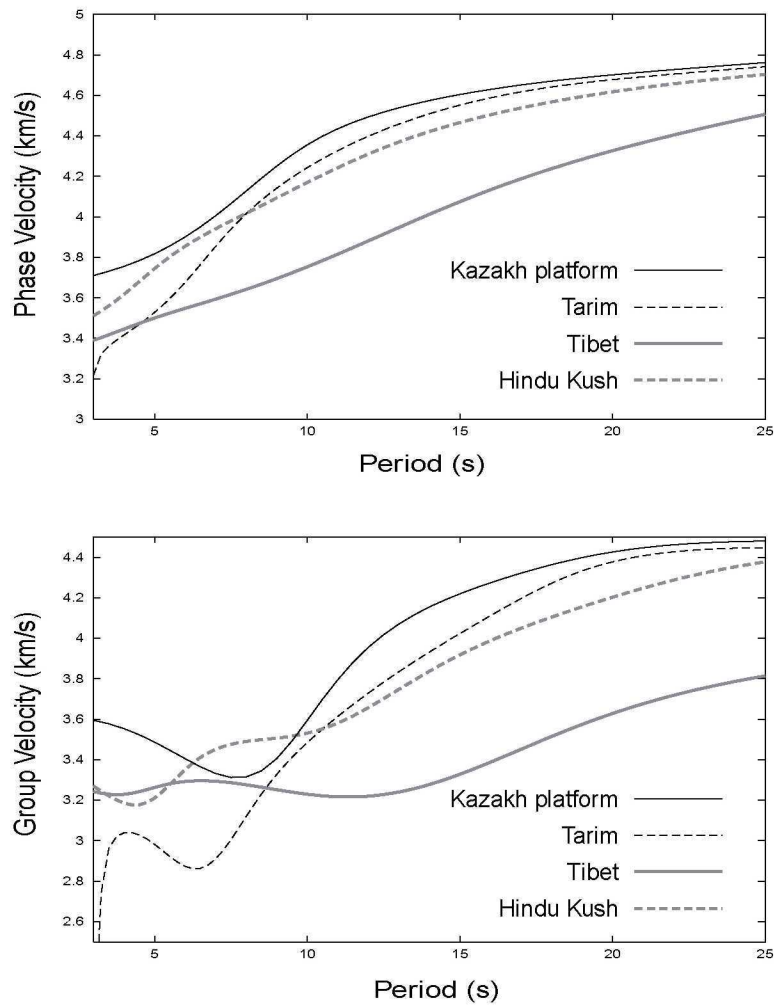
Figure 4: Phase (top) and group (bottom) velocity dispersion curves for the first Rayleigh higher mode for the different geographical locations identified in Figure 2.
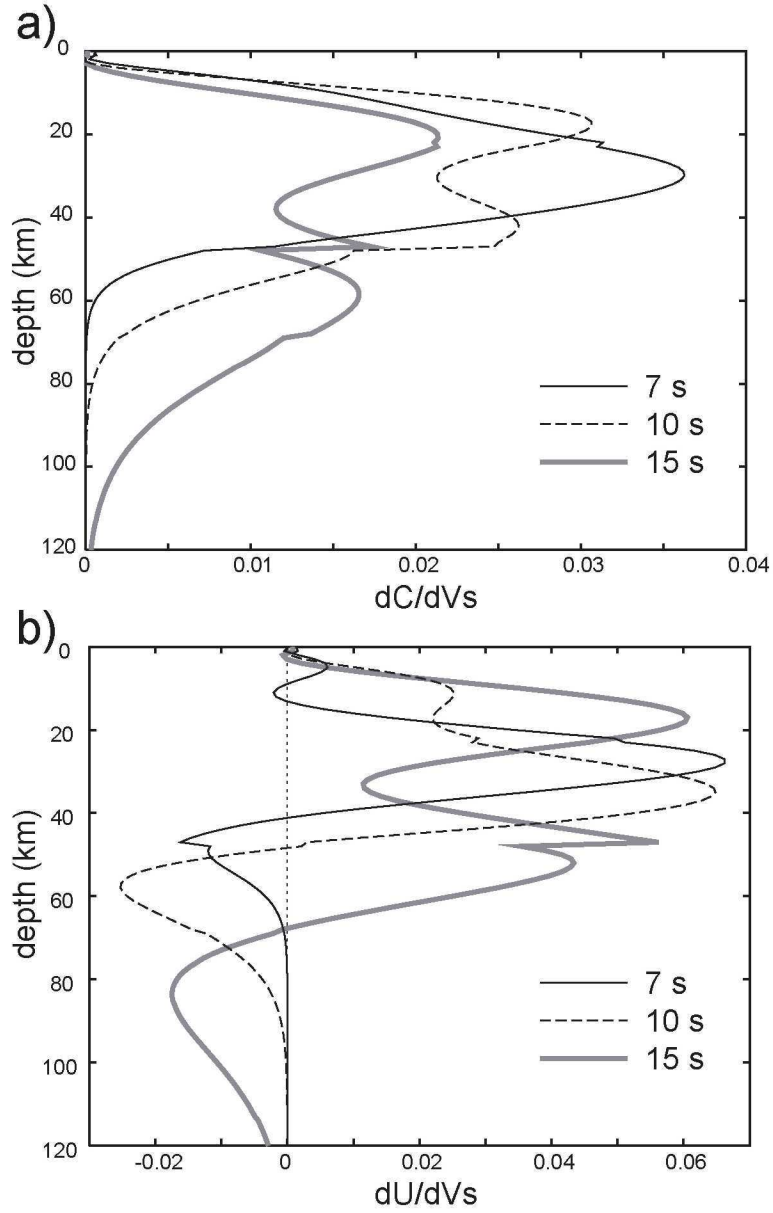
Figure 5: Radial sensitivity kernels to shear velocity for the first Rayleigh higher mode computed for a model of the Tibetan plateau (shown in Figure 2) at the three indicated periods: (a) phase velocity kernels and (b) group velocity kernels.
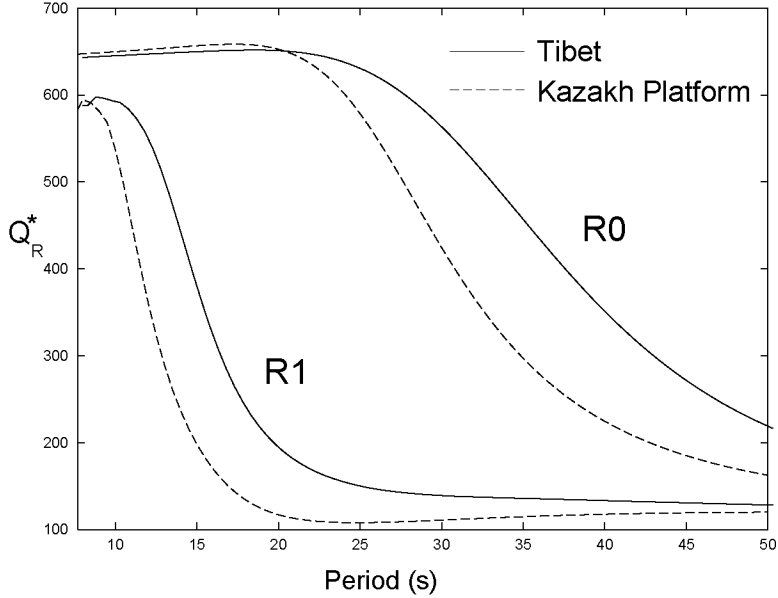
Figure 6: Modal quality factor, Q^*, as a function of period for the fundamental (R_0) and the first higher Rayleigh (R_2) modes for the Kazakh Platform and the Tibetan plateau. Crustal and mantle structure are shown in Figure 2 and the intrinsic Q model is 600 in the crust, and reduces similarly in both regions in the mantle.

eigenfunctions. Figure 6 illustrates how crustal thickness changes Q^*, by plotting $Q^*(T)$ for the first overtone and the fundamental modes at a location in Kazakhstan (typical continental crustal thickness) and Tibet (exceptionally thick crust). The intrinsic Q of the crust in both cases is 600 and Q decreases in the mantle. The values of Q^* between 10 and 15 sec period for the first higher modes are significantly lower than Q^* for fundamental modes at these periods and are close to the values of Q^* for fundamental modes between 25 and 35 sec period. This is one of the reasons why the first overtones are hard to observe, they tend to be obscured by the fundamentals even though they do not directly overlap on the frequency - time diagram. Also, note that Q^* is larger for Tibet than for the Kazakh Platform starting at about 10 sec period. This is due to Tibet's thicker crust which prevents penetration of short period waves into the upper mantle with its lower Q values. The efficiency of excitation of higher modes depends on the depth of the source, the source mechanism, and crustal structure. Although the absolute values of the reflection coefficients for shear waves at the Moho and the free surface are equal to unity, the shear velocity contrast at Moho influences the resulting amplitudes of higher modes as it determines the loss of energy leaked into the mantle. The resulting amplitudes of the higher modes will depend on several factors, including the structure of the medium and the depth and mechanism of the source (Levshin et al., 1972b; Levshin et al., 1989). The radiation pattern of the higher modes is often quite different from that for fundamental modes (Figure 7). Examples of radiation patterns for an event on 03/28/1999 in Southern Tibet are shown in Figure 7 for different source depths. The radiation pattern for the fundamental mode between 8 and 16 sec period has only two lobes, while the radiation pattern for the first higher Rayleigh mode has four lobes for source depth less than 50 km. Similar results are obtained for other source mechanisms and crustal models. The additional nodes in the overtone radiation pattern contributes to the lower chance of its observation relative to fundamental modes. Examples of spectral amplitudes as a function of source depth for fundamental and first higher Rayleigh modes at different periods are presented in Figure 8. The source mechanism is for the
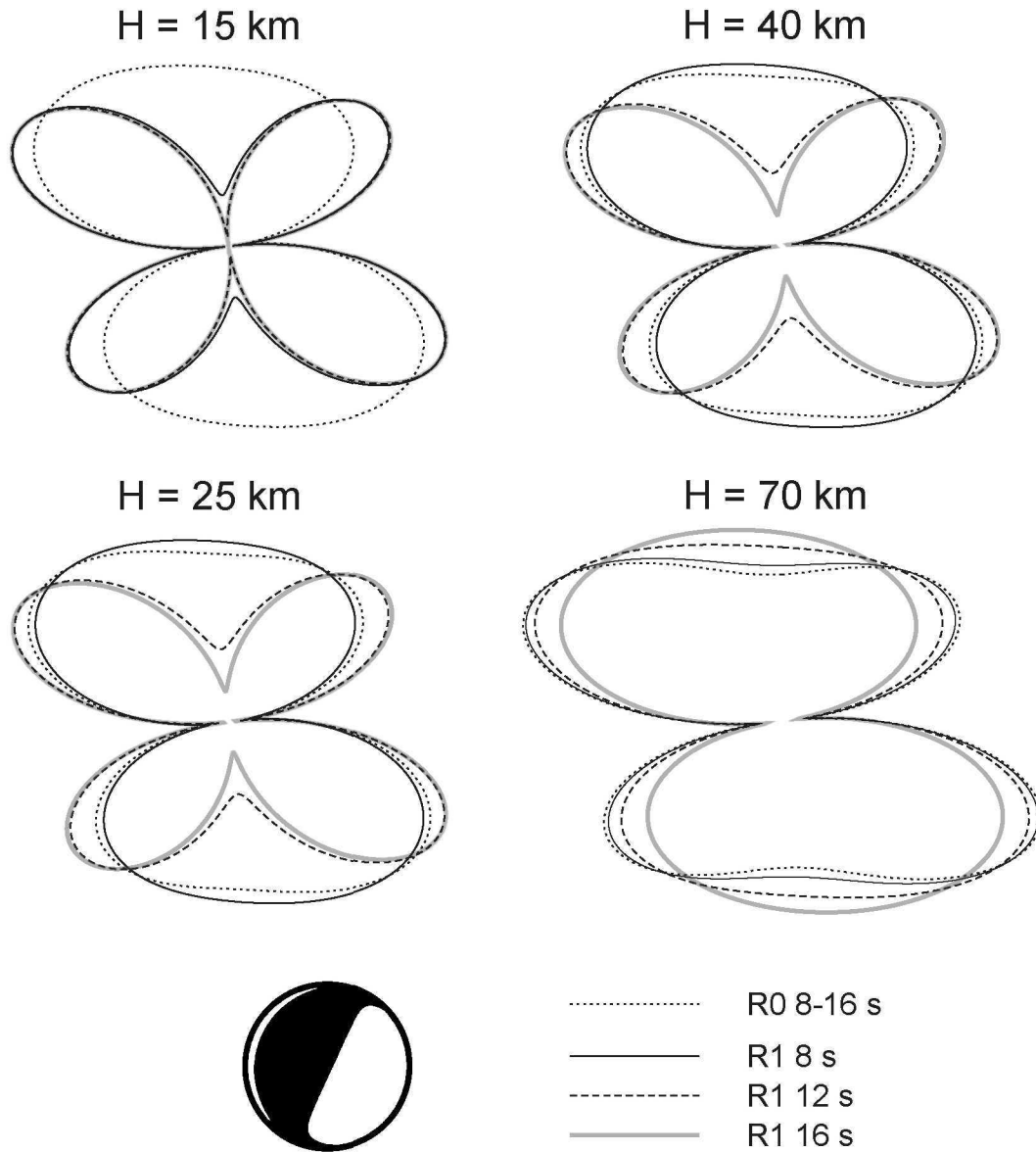
8

Figure 7: Radiation patterns of the fundamental (R_0) and first higher (R_1) Rayleigh modes for the Tibetan plateau model (Fig. 2) at periods from 8 sec to 16 sec. Source depths and the source mechanism are indicated. Higher mode radiation patterns are more likely to display four lobes than the fundamental mode radiation patterns.
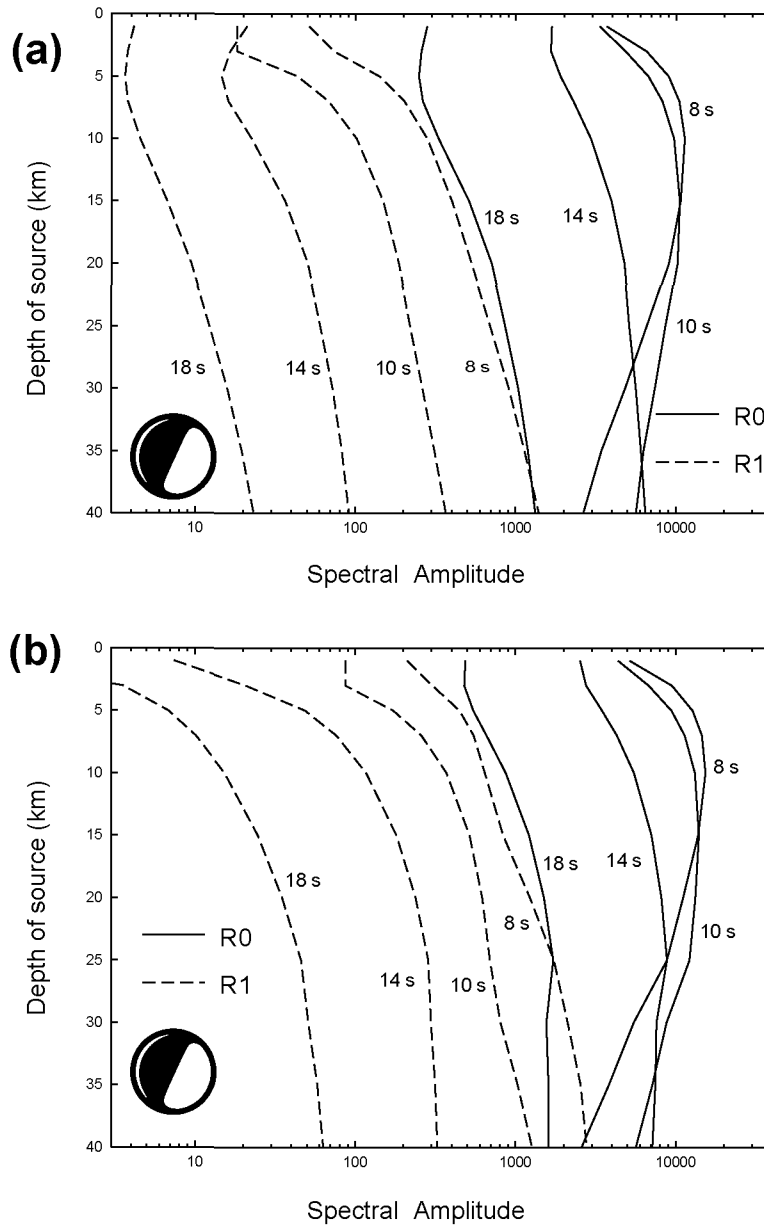
Figure 8: Dependence of the spectral amplitudes of the fundamental and first higher Rayleigh modes on source depth: (a) Tibetan plateau model and (b) Kazakh Platform model from Figure 2. Solid lines represent the amplitudes of the fundamental mode (R_0) and dashed lines are the first higher mode (R_1).

same event in Southern Tibet used to construct Figure 7. Two structural models, namely, for the Tibetan Plateau and for the Kazakh Platform are selected (see Figure 2). Higher modes have significantly smaller amplitudes for shallow events, but their amplitudes grow quickly as the source deepens. This is especially true for the Tibetan structure with the thick crust. The excitation of the higher mode at the same period is more efficient in a model with thick crust. The relative increase in intensity of the higher Rayleigh modes with increasing source depth is well observed on synthetic seismograms for the fundamental and first higher Rayleigh modes for the Tibetan model (Figure 9). For shallow events, the fundamental mode obscures the overtone. With events at 30 km depth or deeper, the amplitude of the first crustal Rayleigh overtone is commensurate with the fundamental mode amplitude, at least for the Tibetan structure. This source depth dependence is different for Love waves, however.

1.2.4 Expected observability of higher modes

In summary, we expect that the first overtone between about 8 sec and 18 sec period will be the best target for observation and will have the greatest relevance to crustal structure and thickness. The exact period band will depend on local structure. These waves are well separated from other interfering waves. The amplitude of the first overtone is expected to be largest in regions with thick crust and following earthquakes that are deeper than the shallow crust. Central Asia is an ideal location to search for these observations, as crust is thick and seismicity deeper than the shallow crust is relatively plentiful.

1.3 Observations

For the reasons discussed above, we limit observations to the Central Asian region extending between $10° − 50°$N and $40° − 120°$E. Concentration is on obtaining group velocity dispersion curves for the first crustal overtone starting at about 5 sec period and extending to about 20 sec. We used broad-band waveforms following earthquakes that occurred between 1977 and 2002 in and around Eurasia recorded at stations from both global networks (GDSN, GSN, GEOSCOPE) as well as temporary regional arrays (e.g., KNET, KAZNET, Saudi Arabian Network, PASSCAL deployments in Tibet and Nepal).

To identify higher modes we used the same FTAN technique that has been used previously for detecting and measuring the dispersion of fundamental modes (e.g., Levshin et al., 1972a, 1989, 1992; Ritzwoller & Levshin, 1998). Higher mode group velocity curves from FTAN diagrams were obtained only when a distinct short-period higher-mode signal was visible (e.g., Figures 10, 11).

The percent of such records relative to records with distinct fundamental mode signals is small, on the order of 3%. Outliers were rejected by comparison with values obtained by ray-tracing through the group velocity maps obtained from the model of Shapiro & Ritzwoller (2002). The number of individual dispersion curves that withstood outlier rejection is shown in Figure 12. The maximum is at periods between about 8 and 15 sec. Figure 13 illustrates the coverage of the region for both Rayleigh and Love first overtones. Coverage is best in Western China, but at the shorter periods extends into Iran in the west, north into Mongolia and Kazakhstan, and east into eastern China. At the longer periods, good path coverage is exclusive to Western China and environs. This is because by 17 sec period, for example, the first higher mode in regions with thinner crust than Tibet strongly samples the mantle and is effectively unobservable. The first crustal overtone
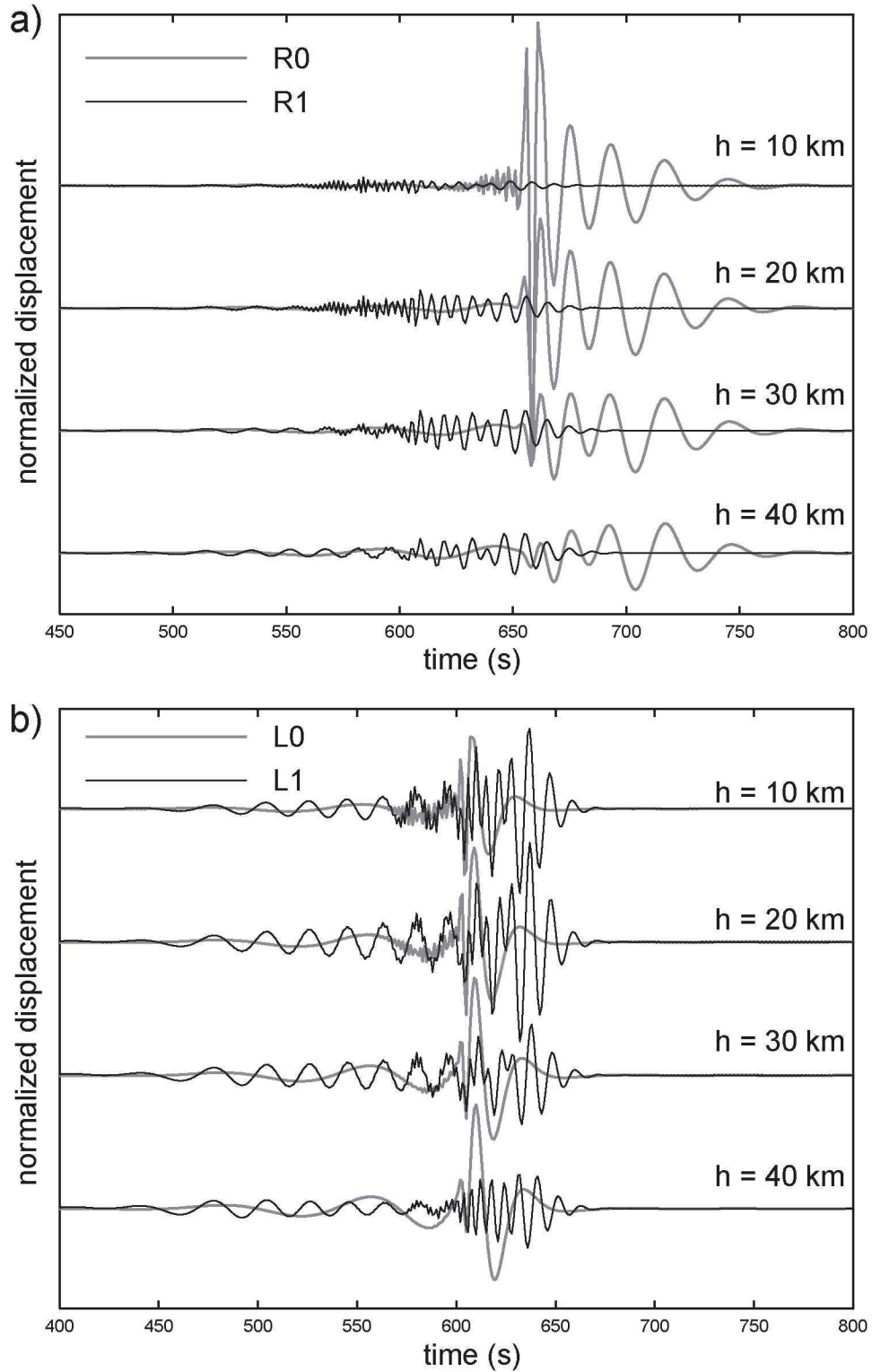
11

Figure 9: Synthetic seismograms of the vertical component of the fundamental (L_0, R_0) and first higher (L_1, R_1) Rayleigh (a) and Love (b) modes for the Tibetan model (Fig. 2) and source depths as indicated. The epicentral distance is 2000 km and the relative magnification o f the seismograms increases by a factor of 1.5 with each depth increment. The source mechanism is shown in Figure 8.
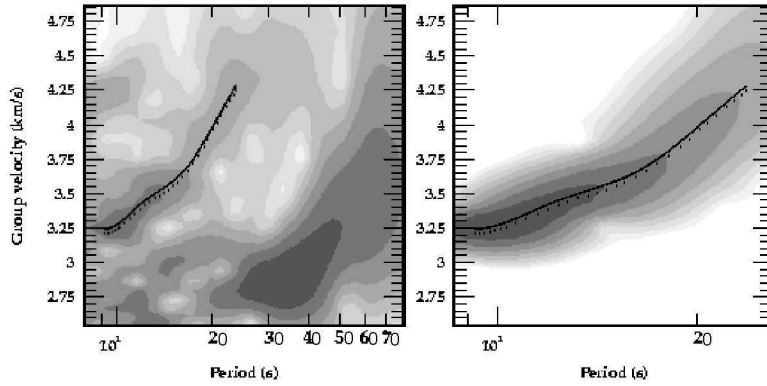
12

Figure 10: Frequency-time (FTAN) diagram for an event in N. Pakistan on May 10, 1992 (depth 33 km, M_s= 5.6) recorded at BUDO (Tibetan Plateau PASSCAL Experiment, 1991-1992, Owens et al., 1993). Epicentral distance is 1890 km. Left: raw FTAN diagram. Right: FTAN diagram for the extracted higher mode
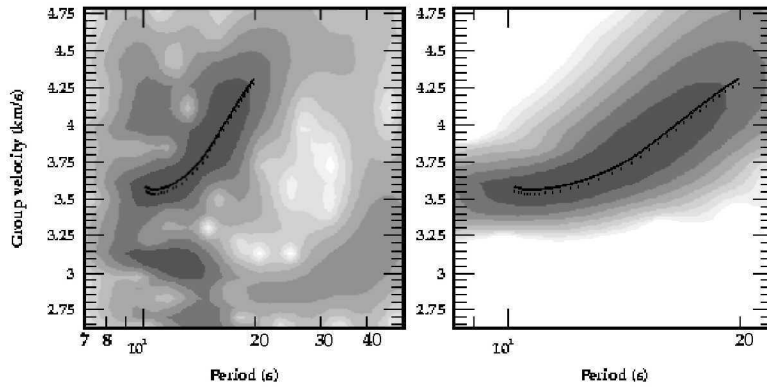

Figure 11: Same as Figure 10, but for an event in the Hindu Kush on October 27, 2001 (depth 96 km, m_b=4.8) recorded at HILE (HIMNT PASSCAL Experiment, 2000-2001, Sheehan et al., 2003). Epicentral distance 1880 km.
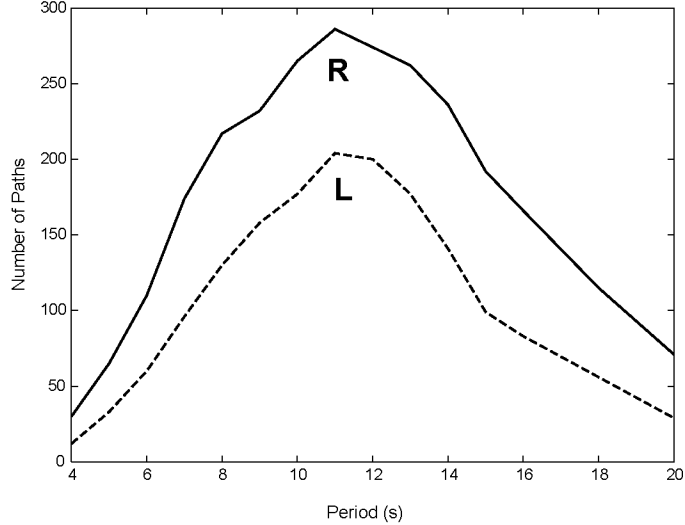
Figure 12: Number of paths for the higher mode measurements as a function of period. Rayleigh - solid line; Love - dashed line.

constraint on crustal structure, therefore, is a broader band and stronger constraint on the Tibetan crust than on the crust in other regions.

1.4   Dispersion Tomography for the First Higher Crustal Mode

Only data at periods between 10 and 17 sec were used to produce the Rayleigh and Love wave dispersion maps. The inversion technique, described by Barmin et al. (2001), was modified to account for the spatially extended frequency-dependent sensitivity of the waves as discussed by Ritzwoller et al. (2002). The use of extended sensitivity kernels has a minimal effect on the estimated maps at these periods, but provides a more accurate estimate of spatial resolution. Spatial resolution is best where data density maximizes (Fig. 13), optimizing at about 500 to 600 km in the region of study. (Resolution is estimated with the method described by Barmin et al., 2001, and is equal the standard deviation of a Gaussian fit to the resolution surface at each location.) The spatial resolution for fundamental modes between 30 sec and 40 sec period where they are most sensitive to the crust is about 250 to 300 km in this region.

Because of the highly variable data distribution, each map is estimated relative to an input reference map. The inversion is constrained to remain near the input map in regions with low path density. We used the group velocity maps for the first higher modes predicted from the 3-D model of Shapiro & Ritzwoller (2002). This highlights areas where the 3-D model needs improvement in the crust. The rms-residual for the reference map is typically 25 - 35 sec, depending on period and wave type. The residual is larger for Love than Rayleigh waves, probably because the Love waves are more sensitive to the upper crust which is poorly known in the reference model. After the inversion, the rms-residuals reduce to values between 18 and 20 sec. Love wave measurements are fit as well as the Rayleigh wave measurements. Because the input reference model fits the Rayleigh overtones measurements better than the Love measurements, the variance reduction is higher for the Love waves, averaging about 60%, whereas the variance reduction for the Rayleigh waves averages about 50%. In both cases, the estimated dispersion maps fit the data much better than the input model.
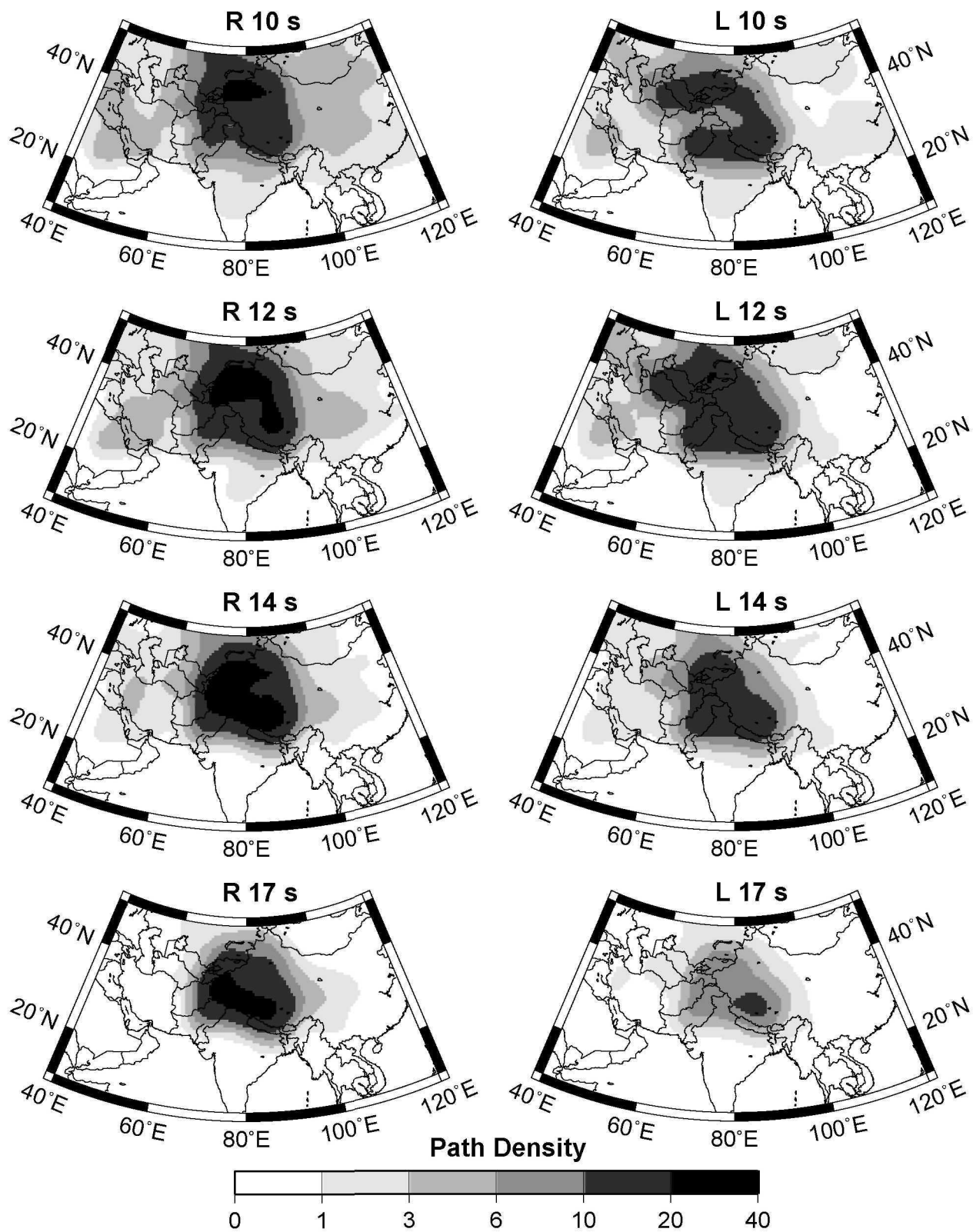
14

Figure 13: Path density for the first higher mode at the indicated periods: Rayleigh mode (left side) and Love mode (right side). Path density is presented as the number of paths crossing each $2° \times 2°$ cell.

The measurements contain significant, new information about crustal structure.

The estimated dispersion maps for Ralyeigh and Love waves at various periods are shown in Figure 14. Figure 15 shows the difference between the estimated map and each input reference map. Comparison between Figures 13 and 15 illustrates that a perturbation in the reference structure is introduced only when there are several paths crossing a $2° \times 2°$ cell. The path density constraint applied here is much weaker than that in our fundamental mode inversions where we require more than 50 paths to intersect a $2° \times 2°$ cell before a perturbation to the underlying structure is introduced. Inspection of Figure 15 reveals that most of the perturbations are negative; that is, the observed waves travel slower than those predicted by the reference 3-D model in most regions and at most periods. The largest negative perturbations are about -400 m/s, which is about a 10% perturbation in group velocity. Figure 14 shows that the spatial variability within each of the maps is considerably larger than $\pm 10\%$. Thus, the input 3-D model proscribes the overall pattern of anomalies expected for the first crustal overtones, but we expect that crustal velocities in the model are, on average, too high and crustal thicknesses in some cases are too small. The inversions in section 5 explore this further. To a fairly good approximation, the patterns of anomalies seen in the continental parts of Figure 14 result from crustal thickness variations in which the thicker crust manifests as low first crustal mode speeds. Tectonically deformed regions have, on average, thicker crust and hence lower crustal overtone speeds relative to adjacent non-tectonic continental crust. Low speeds at short periods in the Caspian and Arabian Seas and the Bay of Bengal result from thick sediments in the model and are largely unconstrained observationally.

1.5   Example Inversions for Crustal Structure

To investigate the information contained in the crustal overtone maps we performed simultaneous inversions of the overtone and fundamental mode maps at two geographical locations that have relatively good coverage by higher modes: the Northern Tien-Shan region (42°N, 74°E) and South-Western China within Tibet (30°N, 100°E). The observed dispersion curves for these two locations are shown as the solid (Rayleigh) and dashed (Love) black lines in the left panels of Figures 16 and 17. There are four observed fundamental mode curves: Rayleigh and Love group (U_0) and phase (C_0) speed. The fundamental mode measurements extend from 16 sec period up to 200 sec period for the Rayleigh wave group speed. There are two observed first overtone curves (U_1) that extend from 10 sec to 17 sec period. The inversions are based on the Monte-Carlo method of Shapiro and Ritzwoller (2002) in which the data are the dispersion curves taken from the dispersion maps at each specified location. Fourteen model parameters describe the crust and upper mantle including the thickness as well as the shear and compressional velocities in each layer of a three-layered crust. The model is isotropic in the crust (although Shapiro et al., 2004 argue that parts of the Tibetan crust is radially anisotropic), but is radially anisotropic in the mantle to a depth of about 200 km and structural perturbations are continuous, being represented by B-splines. Results of the inversion for the two chosen locations are shown in Figures 16 and 17 (right panels). At each depth the full range of models is displayed, defining a corridor of allowed models. The isotropic part of the model in the mantle is shown by taking the average of the V_{sv} and V_{sh} components at each depth and displaying the range of the results. The top pair of panels in each figure shows the inversion without the higher-mode constraint, but shows how the higher mode would be fit if the inversion is constrained only by fundamental mode data. The bottom pair of panels in each figure shows the inversion and fit to all data from the inversion that fits the higher-mode and fundamental mode data simultaneously.
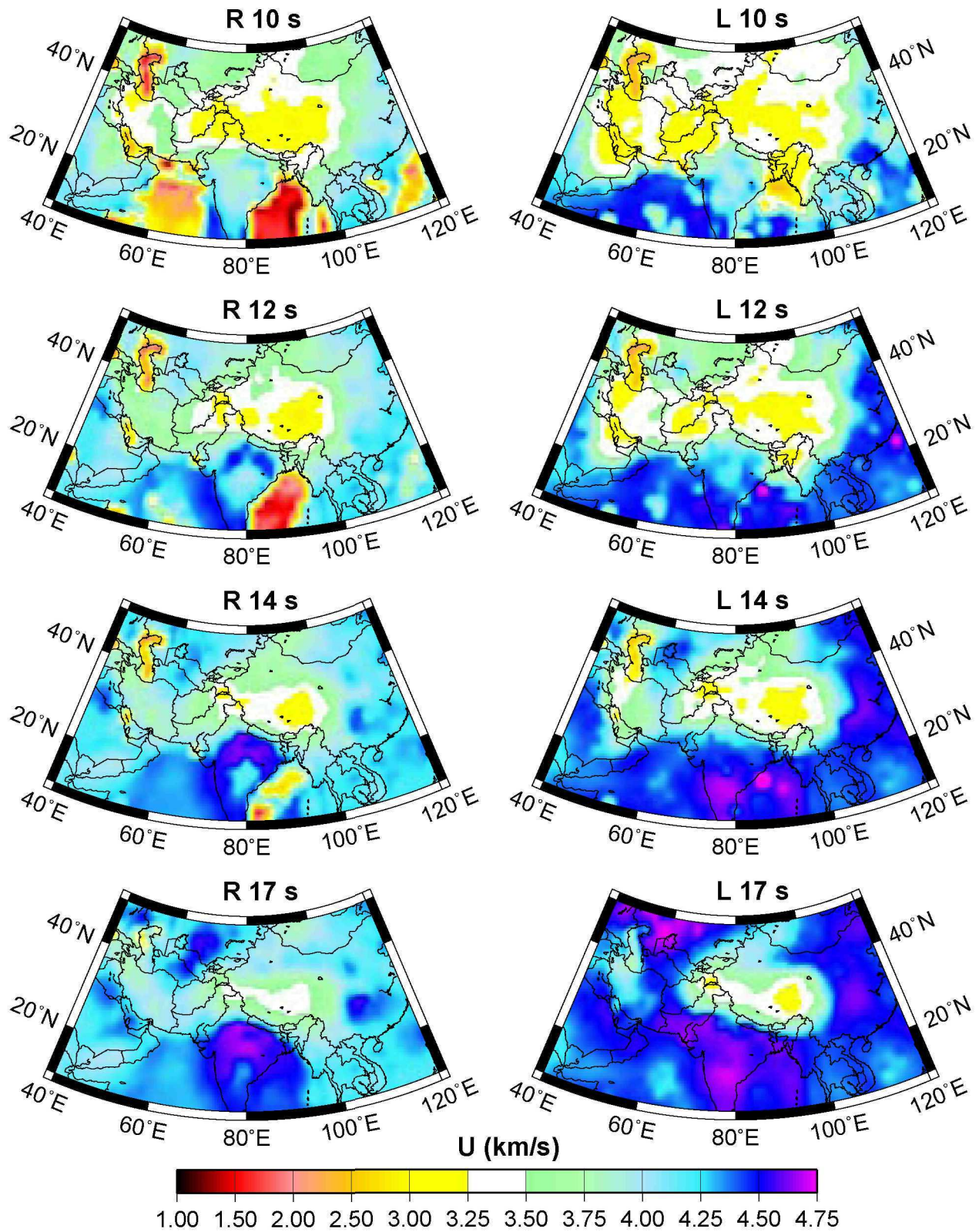
Figure 14: Group velocity maps for the first higher modes at the indicated periods: (left) Rayleigh mode and (right) Love mode.
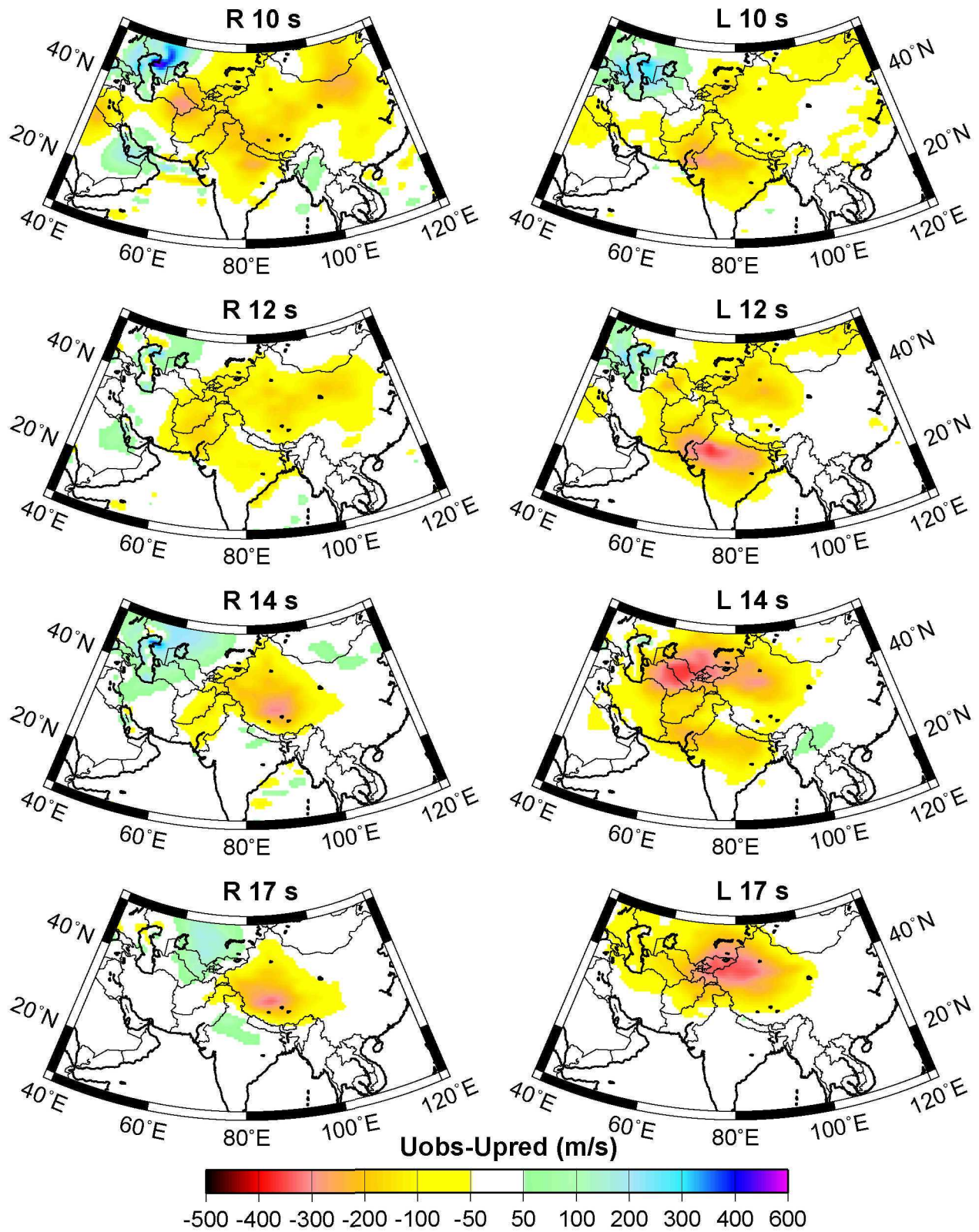
Figure 15: Differential group velocity maps for the first higher modes (observed - predicted) at the indicated periods:(left) Rayleigh mode and (right) Love mode.
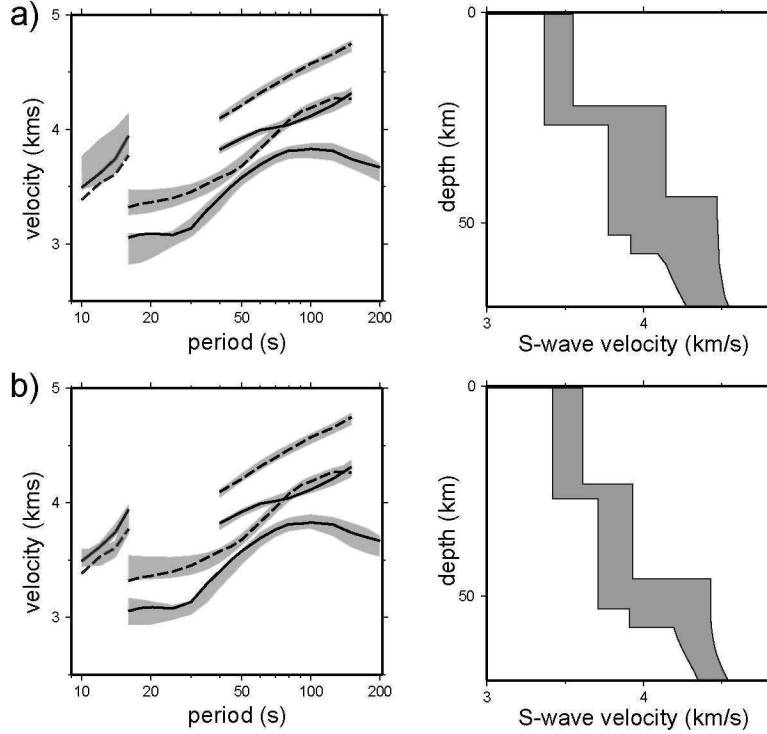
Figure 16: Example of the results of a Monte-Carlo inversion of observed data for a shear velocity profile beneath the Northern Tien-Shan (42°N, 74°E). Left panels display the observed curves as solid (Rayleigh) and dashed (Love) black lines. Rayleigh and Love wave fundamental mode group (U_0) and phase (C_0) velocities are shown together with Rayleigh and Love wave first higher-mode group velocities (U_1). Gray dispersion curves are computed from the range of models shown in the right panel. Right panels display the range of models that fit the data. (a, Top Row) Only fundamental mode data are used in the inversion. (b, Bottom Row) Both fundamental and overtone data are jointly used in the inversion. The joint inversion reduces the range of acceptable models in both the crust and the mantle and reduces the range of crustal thicknesses while fitting all data acceptably.

Figures 16a and 17a demonstrate that without the overtone data in the inversion, the overtone data are poorly fit and the range of models in the crust is large. Including the overtone in the inversion, as shown in Figures 16b and 17b, naturally improves the fit to the overtones but also greatly reduces the range of acceptable models in the crust. This is most dramatic for the Tibetan inversion in which the range of allowed crustal shear velocities and crustal thicknesses is much narrower than if only fundamental mode data are applied.

These results imply that the inclusion of higher-mode observations in inversions for crustal structure significantly improves the crustal part of the model, which is otherwise hard to constrain. In addition, by narrowing the range of admissible crustal models, it also improves the mantle part of the model. It can be seen in Figures 16b and 17b that the range of mantle models also narrows when crustal overtone data are introduced in the inversion. This is not because the overtone data constraint the mantle, however. It is because the range of admissible crustal models has been reduced and the trade-off between crustal and mantle structures has been ameliorated.
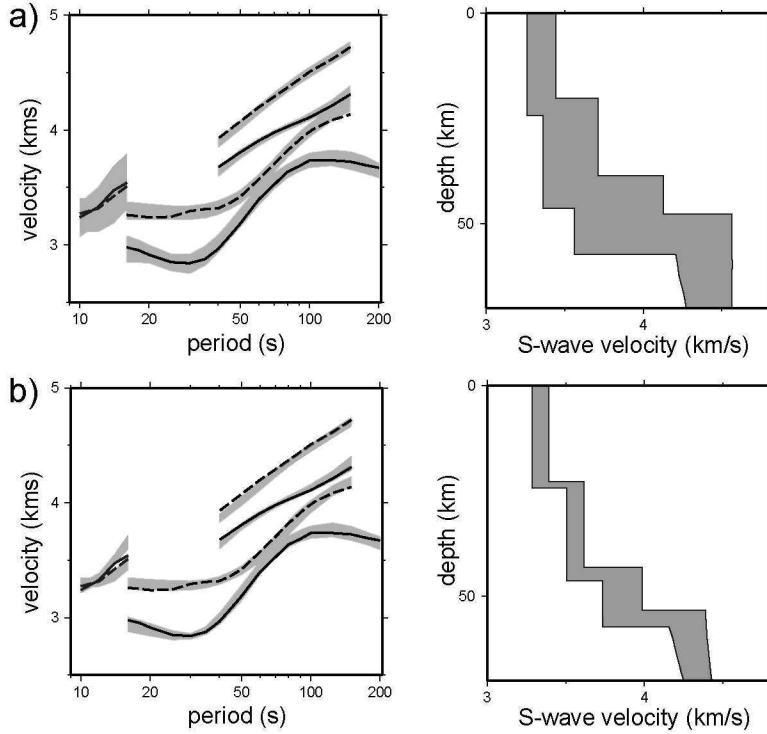
Figure 17: Same as Figure 16, but for a location in South-Western China (30°N, 100°E).

1.6   Conclusions

When reliable measurements of higher crustal modes can be obtained in sufficient number to justify the construction of dispersion maps, they provide valuable information to reduce the range of admissible models of crustal velocities and thickness and help to resolve the trade-off between crustal and mantle structures thereby improving uppermost mantle structures as well. The first higher mode between about 8 sec and 18 sec period is the principal target for reliable travel time estimates. It is best excited by events deeper than the shallow crust and propagates most efficiently in continental regions where crust is thick. For these reasons, we sought measurements of the first higher mode Rayleigh and Love waves in Central Asia and obtained a data set of measurements for about 500 paths across the region. Tomographic maps of the group velocity of the first higher modes provide new information about crustal structure across much of Central and Southern Asia and part of the Middle East. Monte Carlo inversion of first higher-mode and fundamental mode dispersion at several locations show that the higher modes significantly reduce the range of acceptable crustal models and improve the vertical resolution of the crust from the mantle. Further development of the higher-mode data set will permit a general 3-D simultaneous inversion for shear velocity structure of the crust and upper mantle in this region with better vertical resolution than in our existing model (Shapiro and Ritzwoller, 2002).

2 Use of 3D-model for relocation of seismic events

In this section I will describe recent results of application of the 3D global model CUB2 obtained by means of the surface wave tomography for relocation of seismic events. How the model CUB2 was obtained will be discussed at lectures of Professor M. Ritzwoller.

2.1 Conversion of 3D S velocity model to 3D P velocity model

As P waves play dominant role in any location technique it is necessary to convert the obtained S velocity model of the mantle into P velocity model. There are two general approaches to doing this. The first is to use "empirical scaling relations" that convert S-wave anomalies into P-wave anomalies. The most successful of these, map shear-speed perturbations, δv_s, relative to a reference S-model, v_{s_0}, to compressional-velocity perturbations, δv_p, relative to a reference P-model, v_{p_0}, where $d\ln v_p/d\ln v_s$ is then taken to be an empirically constrained constant that may be a function of depth, but is usually depth invariant. The second approach is to use a "theoretical conversion" based on laboratory measurements of thermoelastic properties of mantle minerals and on models of the average mineralogical composition of the mantle. We convert only isotropic v_s to v_p. In the radially anisotropic part of CUB2.0 we, therefore, use $(v_{sv} + v_{sh})/2$.

We prefer the theoretical conversion from v_s to v_p for two reasons. First, as we will show below, the theoretical conversion appears to work somewhat better in that the regional P and P_n empirical phase path anomalies are fit better by travel times predicted by empirical model. Second, the theoretical conversion leads naturally to future improvement. It can be regionally tuned in a physically meaningful way by modifying the mineralogical composition and temperatures within the anelastic model, and it can be updated as better mineralogical data become available.

Figure 18a shows the resulting v_s to v_p theoretical conversion. F igure 18b displays this conversion presented as the logarithmic scaling relation, $d\ln v_s/d\ln v_p$, which varies with both v_s and depth. The v_s profile from AK135 is overplotted, nearly paralleling the contours of the theoretical predictions. This illustrates why depth-independent values of the scaling relation tend to work fairly well in the upper mantle. For the values of v_s in AK135, the theoretical prediction for the scaling relation is $d\ln v_s/d\ln v_p \sim 1.6 - 1.8$. Figure 18b also shows that the v_s profile converted from the AK135 v_p profile by the theoretical conversion agrees fairly well with the v_s profile in AK135 at depths below about 100 km. The theoretical conversion between v_s and v_p differs appreciably from the v_s and v_p p arts of AK135 above about 100 km. Thus, in the shallower parts of the mantle, v_p computed using the theoretical conversion will differ appreciably from v_p computed using the logarithmic scaling relation applied to reference values from the 1-D model AK135 .

Location experiment

Here we present the results of a validation test in which, using the described above 3D model of the crust and upper mantle and regional phase data alone, we relocate ~ 340 earthquakes and nuclear explosions in Eurasia. The event locations using the 3D model are compared with so-called Ground Truth (GT) data, either known by non-seismic means or validated by cluster analysis, with location accuracy mostly 5 km or better. To locate seismic events using only regional Pn and P phases we apply the grid-search technique. A grid 50×50 km with 1 km spacing is built around a reference
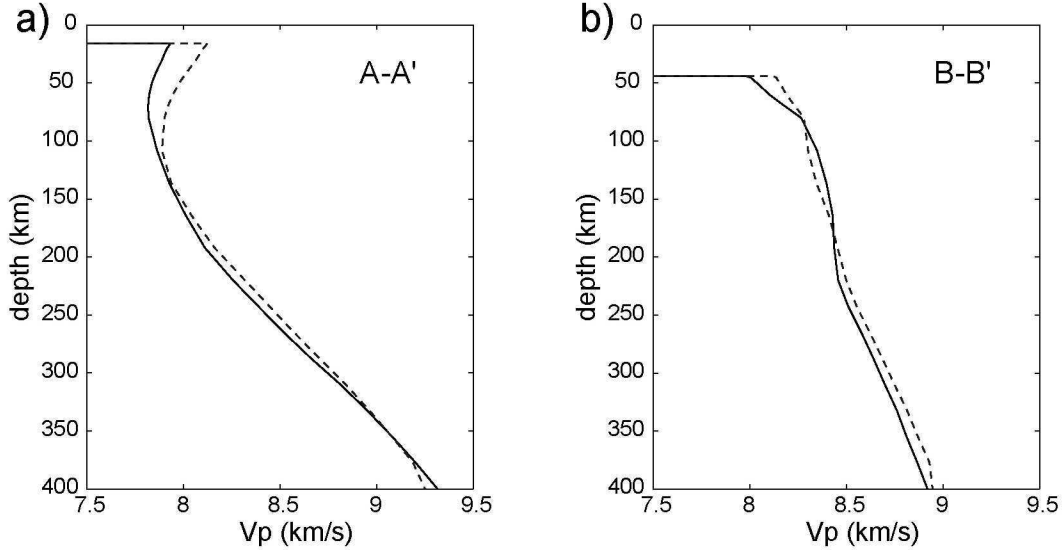
Figure 18: Two examples of v_p model: (a) The Western Mideterranian (b) Eastern Europe. The solid line represents the theoretical conversion from v_s and the dashed line is from the empirical scaling relation $d \ln v_s / d \ln v_p = 2.0$ in which AK135 is used as the reference.

point known from teleseismic information taken from PDE or EHB (Engdahl *et al.*,1998) catalogs. For each point of the grid and each observed arrival we calculate travel times of Pn and P waves as predicted by our model. Travel times for each phase are found using so-called Source Specific Correction Surfaces (SSSCs) which were calculated beforehand for more than 800 seismic stations. Each SSSC is a multi-level table of travel times for Pn and P waves propagating in our 3D model, each level corresponds to a certain source depth and contains travel times on a grid of azimuthal directions from the station to epicentral distances less than 20°. Actually, there are not full travel times but corrections relative to 1D-model (typically, AK135). These corrections are found by 2D ray tracing through the 3D model using technique developed by Červený & Pšenčík (1984). An example of SSSC is shown in Figure 19.

We estimate rms-misfit of predicted and observed travel times for all observed phases in each point of the grid and select the node with minimal rms as a new location (Figure 20). Location errors for 3D and 1D location for explosions on Lop Nor test site in China and earthquakes in Racha seismic zone, Georgia, relative to ground truth locations is shown in Figure 21. One can see strong bias in locations with 1D model.

The statics of relocation for a set of 16 clusters shows significantly better accuracy achieved using 3D location (Tables 1 and 2). Results of random selection e xperiment in which we use for relocation different combinations of n stations f or different values of n show that 3D location produces more accurate results t han 1D location in 70-75% of all cases (for explosions and GT5 earthquakes), if $n \geq 5$. This test indicates that the location of regional events can be significantly improved by using a global 3D model. More details are presented in Levshin & Ritzwoller (2002), Ritzwoller *et al.* (2002b).

22

Travel time corrections (s)
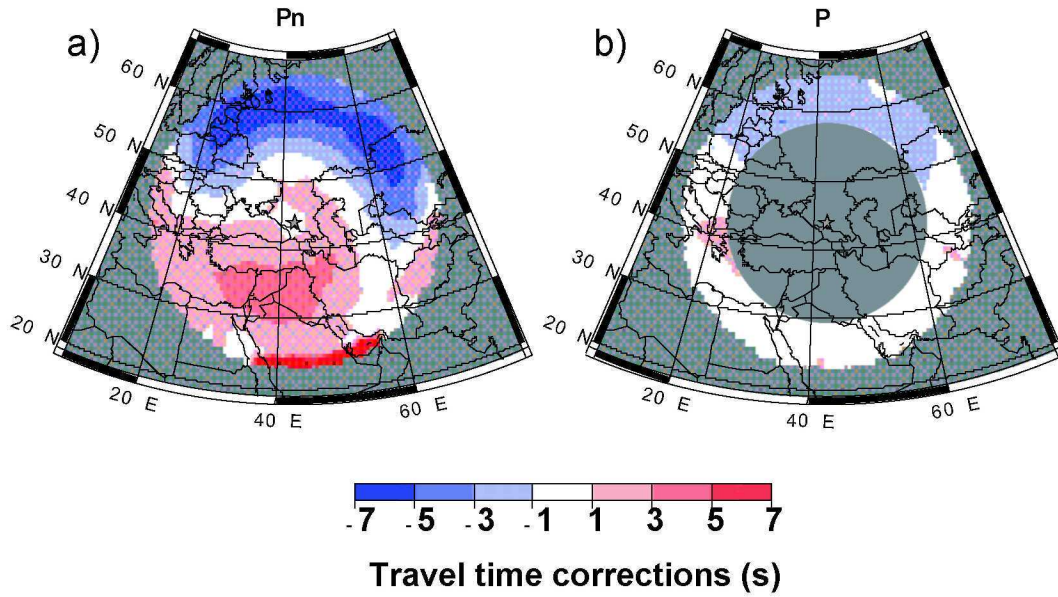
Travel time corrections relative to 1-D model for station KIV (N. Caucasus)

Figure 19: Example of P_n and P travel time correction surfaces computed for a surface source for station KIV. The corrections here are relative to the 1-D model AK135

Table 1. Location results for nuclear explosions.

|				CUB2.0_TH		AK135	
Cluster No.	Name	Events[a]	Stations[b]	Error[c]	RMS[d]	Error[c]	RMS[d]
1	Azgir	6	19	4.2	1.08	24.0	1.49
2	Balapan	10	25	3.9	1.10	11.2	1.22
3	Degelen	3	18	3.1	1.01	12.0	1.36
4	Lop Nor	16	45	6.1	1.22	9.6	1.49
5	Novaya	3	15	8.0	1.03	13.6	1.57
	overall[e]	38	24	5.1	1.09	14.1	1.43

[a]Number of events with open azimuth $< 180°$ and ≥ 5 stations.
[b]Median number of stations.
[c]Average distance from estimated to GT location, in km.
[d]Rms difference between observed and predicted travel times, in sec.
[e]Total or average of cluster values.
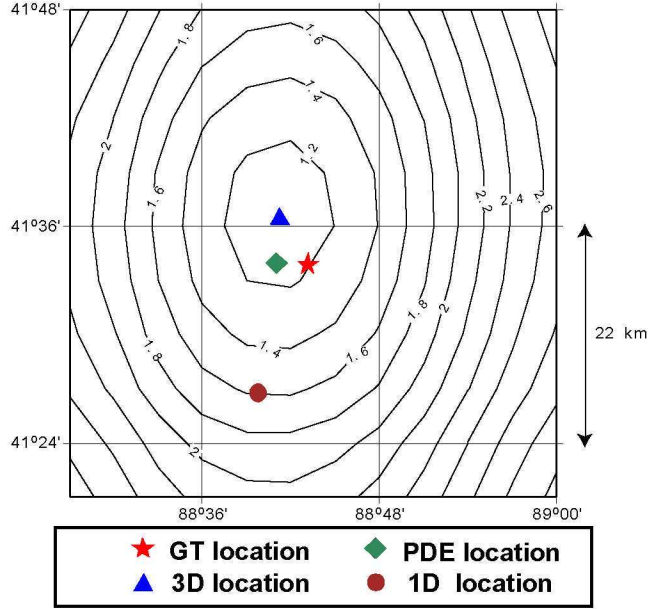
**Example of location using 3D and 1D models and regional data
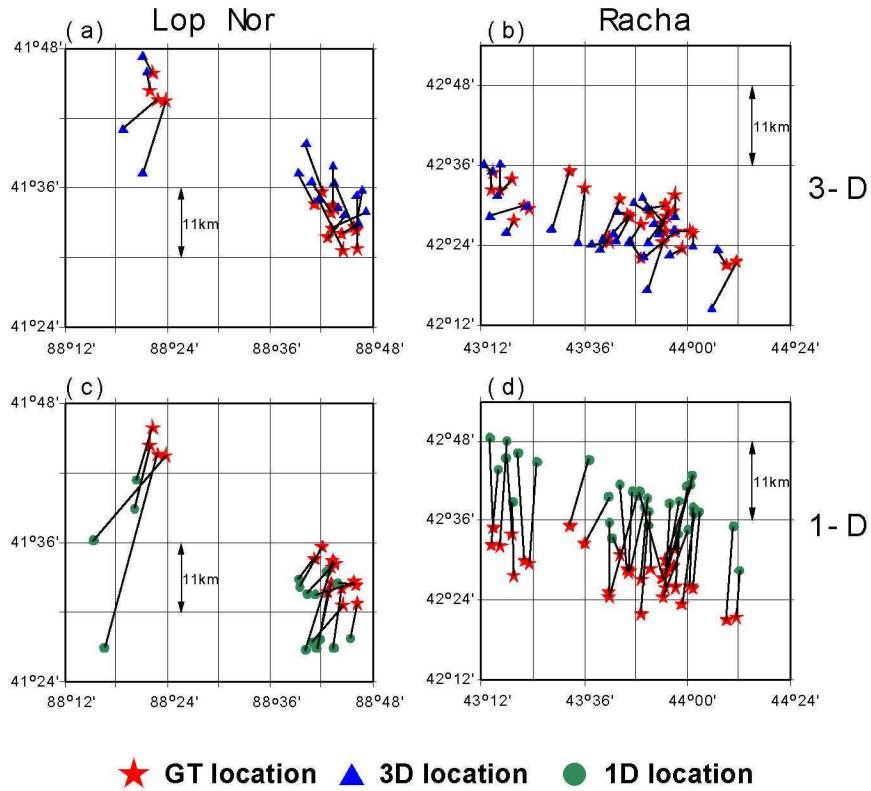for explosion on Lop Nor test site (China)**

Contours are for Rms-misfit in seconds

Figure 20: Contours of rms-misfit using the 3-D model CUB2.0_TH for a grid of hypothesized epicenters for an explosion at the Lop Nor test site (May 26, 1990; 54 reporting stations). Units are seconds. The GT1-2 location is indicated with a star, the best-fit locations using the 3-D and 1-D models are shown with a triangle and a circle, respectively, and the PDE location is shown with a diamond.

Table 2. Location results for GT5 earthquakes.

Terminology similar to Table 1.

Cluster No.	Name	Events	Stations	CUB2.0_TH		AK135	
				Error	RMS	Error	RMS
7	Adana	19	23	8.8	1.04	8.1	1.17
8	Bhuj	4	15	11.5	1.00	8.5	1.42
9	Chamoli	50	17	10.8	1.20	20.8	1.54
10	Duzce	21	45	7.3	1.23	6.6	1.33
11	Erzin	8	33	6.0	1.29	9.5	1.61
12	Garm	26	21	5.2	1.12	9.7	2.17
13	Hoceima	21	26	4.4	0.90	7.5	0.86
14	Izmit	8	116	5.1	1.07	5.3	1.10
15	Koyna	8	10	5.5	1.13	10.7	1.23
16	Racha	34	20	8.2	1.15	21.8	1.43
17	Siberia	8	33	6.3	1.13	11.0	1.31
	overall	207	32	7.2	1.12	10.9	1.38

**Mislocation vectors for two events: an explosion at
Lop Nor (China) and an earthquake ar Racha (Georgia).**

Figure 21: Mislocation vectors from two event clusters for (left column) explosions on the Lop Nor test site and (right column) earthquakes near Racha, Georgia. (a) and (b) 3-D model (CUB2.0_TH) locations. (c) and (d) 1-D model (AK135) locations. Stars mark GT locations, triangles and circles are 3-D and 1-D model locations, respectively.

Conclusions

Two main characteristics of our global model of the crust and upper mantle distinguish it from previous global tomographic models. First, both vertical and lateral resolution are improved as a result of inverting a new broad-band data set of group and phase velocities and the use a-priori information to restrict the range of physically plausible models. A novel characteristic of the data set is the use of a large number of group velocity measurements for both Rayleigh and Love waves.

References

Alexander, S.S., 1962. A Study of the Normal Modes of Surface Waves Across the Western United States, *J. geophys. Res.*, **67**, 3537-3538.

Barmin, M.P., Levshin, A.L., & Ritzwoller M.H., 2001. A fast and reliable method for surface wave tomography, *Pure Appl. Geophys.*, **158**, 1351-1375.

Bourjot, L. & Romanowicz, B., 1992. Crust and upper mantle tomography in Tibet using surface waves, *Geophys. Res. Lett.*, **19**, 881-884.

Brune, J. & Dorman, J., 1963. Seismic waves and Earth structure in the Canadian shield, *Bull. seismol. Soc. Am.*, **53**, 167 - 210.

Červený, V., and I. Pšenčík, SEIS83 – Numerical modeling of seismic wave fields in 2-D laterally varying layered structures by the ray method, *Documentation of earthquake algorithms, Report SE-35*, E.R. Engdahl (ed.), pp. 36-40, Boulder: World Data Center A for Solid Earth Geophysics, 1984.

Crampin S., 1964. Higher modes of seismic surface waves: preliminary observations, *Geophys. J. R. astr. Soc.*, **9**, 35 -37.

Crampin, S., 1966a. Higher modes of seismic surface waves: propagation in Eurasia, *Bull. seism. Soc. Am.*, **56**, 1227 - 1239.

Crampin, S., 1966b. Higher-mode seismic surface waves from atmospheric nuclear explosions over Novaya Zemlya, *J. geophys. Res.*, **71**, 2951-2958.

Crampin, S. & King, D., 1977. Evidence for anisotropy in the upper mantle beneath Eurasia from the polarization of higher mode seismic surface waves, *Geophys. J. R. astr. Soc.*, **49**, 59-85.

Curtis, A. & Woodhouse, J.H., 1997. Crust and upper mantle structure beneath the Tibetan plateau and surrounding regions from interevent surface wave inversion, *J. geophys. Res.*, **102**, 11,789-11,813.

Ekström, G., Tromp, J., & Larson, E.W.F., 1997. Measurements and global models of surface waves propagation, *J. geophys. Res.*, **102**, 8137-8157.

Engdahl, E. R., R. van der Hilst, and R. Buland, 1998. Global teleseismic earthquake relocation with improved travel time and procedures for depth determination, *Bull. Seismol. Soc. Am.*, **88**, 722 - 743.

Ewing W.M., Jardetzky, W.S., & Press F., 1957. *Elastic waves in layered media*, McGraw-Hill Book Co.

Friederich W., 2003. The S-velocity structure of the East Asian mantle from inversion of shear and surface wave forms. *Geophys. J. Int.*, **153**, 88-102.

Gabriels, P., Snieder R., & G. Nolet, 1987. In situ measurements of shear velocity in sediments with higher mode Rayleigh waves, *Geophys. Prosp.*, **35**, 187-196, 1987

Griot, D.-A., Montagner, J.-P., & P. Tapponnier, 1998. Phase velocity structure from Rayleigh and Love waves in Tibet and its neighboring regions, *J. geophys. Res.*, **103**, 21,215- 21,232.

Huang, Z., Su, W., Peng, Y., Zheng, Y., & Li, H., 2003. Rayleigh wave tomography of China and adjacent regions, *J. geophys. Res.*, **108**, 2073, doi:10,1029/2001JB001696.

Kennett, B.L.N., Engdahl, E.R., & Buland, R., 1995. Constraints on seismic velocities in the Earth from travel times, *Geophys. J. Intl'*, **122**, 403-416.

Kovach R.L. & Anderson, D.L., 1964. Higher mode surface waves and their bearing on the structure of the earth's mantle, *Bull. seismol. Soc. Am.*, **54**, 161 -182.

Lebedev, S. & Nolet, G., 2003. Upper mantle beneath Southeast Asia from S velocity tomography, *J. geophys. Res.*, **108**, doi:10.1029/2000JB000073.

Levshin, A.L., Pisarenko, V.F., & Pogrebinsky, G.A., 1972a. On a frequency-time analysis of oscillations. *Ann. Geophys.*, **28**, 211-218.

Levshin, A.L., Frantsuzova, V.I., & Shkadinskaya, G.V., 1972b. Higher modes of Rayleigh waves and upper mantle structure. In *Comput. Seismology*, (ed. Keilis-Borok V.I.), Consult. Bureau, N.Y. - London, 93-100.

Levshin, A.L., Yanovskaya, T.B., Lander, A.V., Bukchin, B.G., Barmin, M.P., Ratnikova, L.I., & Its, E.N., 1989. *Seismic Surface Waves in Laterally Inhomogeneous Earth*. (Ed. V. I. Keilis-Borok), Kluwer Publ. House, Dordrecht/ Boston/ London.

Levshin, A.L., Ratnikova, L.I., & Berger, J., 1992. Peculiarities of surface wave propagation across the Central Eurasia. *Bull.seism. Soc. Am.*, **82**, 2464-2493.

Levshin, A.L., and M.H. Ritzwoller, 2002. Application of a global-scale 3D Model to improve regional locations, Studia Geoph. et Geod., **46**, 2, 289-292.

Levshin, A.L., M.H. Ritzwoller, and N.M. Shapiro, 2004. The use of crustal higher modes to constrain crustal structure across Central Asia. Submitted to *Geophys. J. Int.*, April 2004.

Nolet, G., 1975. Higher Rayleigh modes in Western Europe, *Geophys. Res. Lett.*, **2**, 60-62.

Nolet, G., 1977. The upper mantle under Western Europe inferred from the dispersion of Rayleigh modes, *J. Geophysics*, **43**, 265-285.

Nolet, G., 1978. Simultaneous inversion of seismic data, *Geophys. J. Roy. astr. Soc.*, **55**, 679-691.

Nolet, G., 1987. Waveform Tomography, in: *Seismic Tomography*, G. Nolet (ed.), Reidel, Dordrecht, 301-322.

Officer, C.B., 1958. *Introduction to the theory of sound transmission*, McGraw-Hill Co., N.Y.

Oliver, J., 1962. A summary of observed surface wave dispersion. *Bull. seismol. Soc. Am.*, **52**, 81-86.

Oliver J., J. Dorman, and G. Sutton, 1959. The second shear mode of continental Rayleigh waves. *Bull. seismol. Soc. Am.*, **49**, 379 -389.

Oliver J. and M. Ewing, 1957. Higher modes of continental Rayleigh waves. *Bull. seismol. Soc. Am.*, **47**, 187-204.

Oliver J. and M. Ewing, 1958. Normal modes of continental Rayleigh waves. *Bull. seismol. Soc. Am.*, **48**, 33-49.

Owens, T.J., Randall, G.E., Wu, F.T., & Zeng, R.S., 1993. PASSCAL Instrument performance during the Tibetan Plateau passive seismic experiment, *Bull. seismol. Soc. Am.*, **83**, 1959-1970.

Ritzwoller, M.H. & Levshin, A.L., 1998. Surface wave tomography of Eurasia: group velocities, *J. geophys. Res.*, **103**, 4839-4878.

Ritzwoller, M.H. & Levshin, A.L., 2002. Estimating shallow shear velocities with marine multi-component seismic data, *Geophysics*, **67**, 1991-2004.

Ritzwoller, M.H., Levshin, A.L., Ratnikova, L.I., & Egorkin, A.A., 1998. Intermediate period group velocity maps across Central Asia, Western China, and parts of the Middle East, *Geophys. J. Int.*, **134**, 315-328.

Ritzwoller, M.H., Shapiro, N.M., Barmin, M.P., & Levshin, A.L., 2002, Global surface wave diffraction tomography, J. geophys. Res., **107** , B12,2335,doi:10.1029/2002JB001777,2002

Shapiro, N.M. & Ritzwoller, M.H., 2002. Monte-Carlo inversion for a global shear velocity model of the crust and upper mantle, *Geophys. J. Int.*, **151**, 88-105.

Ritzwoller, M.H., N.M. Shapiro, A.L. Levshin, E.A. Bergman, E.A. Engdahl, 2003. The ability of global models to locate regional events, J. Geoph. Res., 1 08(B7), 2353,doi:10.1029/2002JB002167, 2003.

Sheehan, A.F., Wu, F.T., Blume, F., Monsalve, G., Gilbert, H., de la Torre, T., Bendick, R., Schulte-Pelkum, V., Bilham, R., Huang, G.C., Pandey, M.R., & Liu, H.B., 2002. Himalayan Nepal Tibet broadband seismic experiment (HIMNT), *Eos Trans.*, **83**, Am. Geophys. Union, Fall Meet. Suppl., Abstract S61D-11.

and Rayleigh waves between 40 and 150 s period, *Geophys. J. Int.*, **122**, 675-690.

van Heijst, H.J. & Woodhouse, J.H., 1999. Global high-resolution phase velocity distribution of overtone and fundamental-model surface waves determined by mode branch stripping, *Geophys. J. Int.*, **137**, 601-620.